Bioactive Materials 40 (2024) 74–87

Contents lists available at ScienceDirect

Bioactive Materials

journal homepage: www.keaipublishing.com/en/journals/bioactive-materials

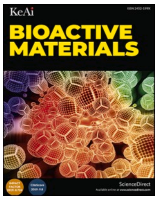

Radiopaque FeMnN-Mo composite drawn filled tubing wires for braided absorbable neurovascular devices

Adam J. Griebel [a,*,1], Petra Maier [b,1], Henry Summers [c], Benjamin Clausius [b], Isabella Kanasty [d], Weilue He [d], Nicholas Peterson [e], Carolyn Czerniak [f], Alexander A. Oliver [g], David F. Kallmes [g], Ramanathan Kadirvel [h], Jeremy E. Schaffer [a], Roger J. Guillory II [f]

[a] *Fort Wayne Metals, Fort Wayne, IN, USA*
[b] *School of Mechanical Engineering, Stralsund University of Applied Sciences, Stralsund, DE, USA*
[c] *Department of Materials Science and Engineering, Michigan Technological University, USA*
[d] *Department of Biomedical Engineering, Michigan Technological University, USA*
[e] *Department of Biological Sciences, Michigan Technological University, USA*
[f] *Joint Department of Biomedical Engineering, Medical College of Wisconsin, Marquette University, USA*
[g] *Department of Radiology, Mayo Clinic, Rochester, MN, USA*
[h] *Department of Neurosurgery, Mayo Clinic, Rochester, MN, USA*

ABSTRACT

Flow diverter devices are small stents used to divert blood flow away from aneurysms in the brain, stagnating flow and inducing intra-aneurysmal thrombosis which in time will prevent aneurysm rupture. Current devices are formed from thin (~25 μm) wires which will remain in place long after the aneurysm has been mitigated. As their continued presence could lead to secondary complications, an absorbable flow diverter which dissolves into the body after aneurysm occlusion is desirable. The absorbable metals investigated to date struggle to achieve the necessary combination of strength, elasticity, corrosion rate, fragmentation resistance, radiopacity, and biocompatibility. This work proposes and investigates a new composite wire concept combining absorbable iron alloy (FeMnN) shells with one or more pure molybdenum (Mo) cores. Various wire configurations are produced and drawn to 25–250 μm wires. Tensile testing revealed high and tunable mechanical properties on par with existing flow diverter materials. In vitro degradation testing of 100 μm wire in DMEM to 7 days indicated progressive corrosion and cracking of the FeMnN shell but not of the Mo, confirming the cathodic protection of the Mo by the FeMnN and thus mitigation of premature fragmentation risk. In vivo implantation and subsequent μCT of the same wires in mouse aortas to 6 months showed meaningful corrosion had begun in the FeMnN shell but not yet in the Mo filament cores. In total, these results indicate that these composites may offer an ideal combination of properties for absorbable flow diverters.

1. Introduction

Cardiovascular disease has proven to be the leading cause of death and disability, affecting at least 126 million individuals worldwide [1]. In the US, it is prevalent in 49.2 % of the population >20 years of age [2]. Due to the temporary nature of vascular remolding and healing, it has been widely accepted that the long-term presence of vascular scaffolds is not required and that the permanent presence of metallic implants may have deleterious long term effects [3–5]. Absorbable metals are poised to improve long term recovery from cardiovascular disease by providing percutaneous delivery of mechanically capable, biocompatible scaffolds that are fully absorbable within the specified time frames determined by the treatment indication [6]. New metal materials that are absorbable and biocompatible are under constant development, which are predominately based on Fe, Mg, Zn, and Mo alloy systems [7–11]. To date, absorbable metals have shown promise for adult coronary, pediatric pulmonary, adult peripheral vascular stents, and adult biliary stents [12]. Smaller vascular anatomies, like the neurovascular space, require smaller devices and present unique challenges for absorbable metals.

Peer review under responsibility of KeAi Communications Co., Ltd.

* Corresponding author. Research & Development, Fort Wayne Metals, Fort Wayne, IN, 46809, USA.

E-mail addresses: adam_griebel@fwmetals.com (A.J. Griebel), petra.maier@hochschule-stralsund.de (P. Maier), hdsummer@mtu.edu (H. Summers), benjamin.clausius@hochschule-stralsund.de (B. Clausius), itkanast@mtu.edu (I. Kanasty), weilueh@mtu.edu (W. He), nbpeters@mtu.edu (N. Peterson), cczerniak@mcw.edu (C. Czerniak), oliver.alexander@mayo.edu (A.A. Oliver), Kallmes.David@mayo.edu (D.F. Kallmes), Kadir@mayo.edu (R. Kadirvel), Jeremy_schaffer@fwmetals.com (J.E. Schaffer), rguillory@mcw.edu (R.J. Guillory).

[1] Co-first author.

https://doi.org/10.1016/j.bioactmat.2024.06.002
Received 31 January 2024; Received in revised form 2 May 2024; Accepted 1 June 2024

Available online 7 June 2024
2452-199X/© 2024 The Authors. Publishing services by Elsevier B.V. on behalf of KeAi Communications Co. Ltd. This is an open access article under the CC BY-NC-ND license (http://creativecommons.org/licenses/by-nc-nd/4.0/).

Absorbable materials have recently been suggested for use in a challenging neurovascular application, wherein flow diverting stents (FD's) are used to treat intracranial aneurysms [13]. FD's are placed in the parent artery over the aneurysm neck and function by diverting blood flow away from the aneurysm. This causes blood stagnation and clotting within the aneurysm sac and the device acts as a bridge for cells to grow over the aneurysm neck, ultimately leading to its occlusion [14]. Flow diverters are fundamentally distinct from balloon expandable stents in that they possess ultrathin wires ~25 μm in diameter which are braided into a tubular structure and can be deployed in a self-expanding manner [15–18]. Potential benefits for using an absorbable material platform for FD's include reduced: side branch occlusion, chronic inflammation, imaging artifacts, and device induced thrombosis. To date, most absorbable FD's have been fabricated from polyglycolic acid (PGA), poly-l-lactic acid (PLLA), and polycaprolactone (PCL) based polymers. High molecular weight PLLA based FD's have been able to exert radial force values similar to commercial flow diverters when built with occlusively large struts (40–45 μm) to compensate for reduced elastic moduli (2–5 GPa) compared to metals, and/or containing non-absorbable radiopaque wires within the braid [13,19–21]. The large struts required by polymers present a host of technical challenges; an absorbable device which is in line with the geometry of existing non-absorbable metallic devices would greatly enhance the applicability. Absorbable metals may allow for such a construction.

It is critical that a deployed FD not only achieve tight apposition to the vessel wall after implantation but also remain patent over time. These performance features depend largely on the flow diverters' conformability and the radial force that is exerted at the deployment diameter. Braided stent mechanical performance is intricately tied to stent design parameters such as wire diameter, braiding angle, open vs. closed loop configuration, and wire element friction, all of which have been the target of numerous finite element modeling studies to optimize complex design parameters [16,22–24]. While braiding design greatly affects the device performance, there are material properties that affect the mechanical performance of braided stents such as stiffness (elastic modulus), and elasticity [25]. A relatively high material elastic modulus provides greater radial force for a given geometry. High elasticity allows for greater wire flexion without permanent deformation during crimping and deployment, key to self-expansion. In conventional materials, elasticity is closely approximated by the ratio of yield strength to elastic modulus. Current cobalt-chrome alloys, which are used in FD's such as the Pipeline Embolization Device (Medtronic) [26], possess moduli values between 200 and 240 GPa and yield strengths exceeding 2000 MPa, providing elastic strains on the order of 1 % [27]. In non-linear materials like nitinol, elasticity is driven by a phase transformation and can exceed 8 % [28]. Nitinol's superelasticity can greatly expand the structural design space, facilitating a closed loop design [29] (e.g. FRED), while conventional materials with lower elasticity may benefit from an open loop configuration [26]. If these properties are not achievable for absorbable materials, considerable design efforts will be necessary to mitigate material shortcomings.

Iron (Fe) has the potential to reach these mechanical benchmarks, and has re-emerged recently in clinical studies as a promising absorbable material candidate for endovascular stents [30]. Initial Fe stents suffered from degradation rates that were too slow, requiring considerable acceleration in order to achieve full absorption between 1 and 2 years [31,32]. Critically, uncoated Fe stents in porcine arteries maintain metallic structure up to 5 years, with continued resorption through 7 years [33]. Despite resorption rate drawbacks, Fe stents have made their way to the clinic in the form of the nitrided iron coronary scaffold (IBS) [34,35]. The scaffold applies an acidic PLDLLA coating with a buffer layer in order to tune biocorrosion, alongside use of reduced material cross section by using 53 μm strut sizes [36]. With this significant advancement, balloon expandable Fe stents in the clinic have been able to achieve degradation within 2–3 years in human vessels. Investigations of iron alloys have primarily focused on the FeMn system; Mn content in the range of 20–35 wt% provides excellent mechanical properties and a stable austenitic structure with reduced magnetic susceptibility [37,38]. Early work with Fe35Mn wire showed promising mechanical and cytocompatibility properties [39], but the wires suffered from premature fracture due to corrosion-assisted cracking. A small addition of nitrogen to the alloy was found to greatly reduce, but not eliminate, this cracking tendency [40].

Our research team has explored Fe-35Mn-0.15 N materials (from here referred to as FeMnN) as potential candidates for absorbable FD's [41]. On the benchtop, FeMnN and magnesium alloy WE22 (Mg-2Y-1.5Nd-0.5Zn) FD's were able to divert flow, functionally corrode, and were compatible with MR imaging [42]. Overall, FeMnN performed better in flow diversion function, in vitro corrosion, and radial force. Although promising, Fe based absorbable materials suffer from premature fracture and low radiopacity at such thin wire diameters, which is required to deploy these endovascular devices under fluoroscopic guidance. Radiopacity of metals is a function of density, atomic number, and material thickness [43]. Presently, Fe and Mg scaffolds that are being tested in the clinic possess non absorbable radiopaque markers to assist in device visualization and deployment, such as tantalum or platinum [13,44]. These permanent metallic markers negate the full absorbable function of the devices, leaving behind their non-absorbable radiopaque markers, which could potentially become sites of chronic inflammation/smooth muscle cell stimulation. Incorporation of fully absorbable and radiopaque components into FeMnN wires could eliminate the need for such permanent markers.

Composite drawn filled tubing (DFT®) wire, with concentric layers of dissimilar metals, has been used in the medical device industry for decades [45] most commonly with a shell of CoNiCrMo 35N LT® alloy and a core of Ag (35N LT-DFT-Ag). This combination provides an excellent combination of fatigue resistance and conductivity and is prevalent in biostimulation leads used in pacing, defibrillation, and deep brain stimulation. A more recently introduced DFT construction has a superelastic nitinol shell and a platinum core, providing a wire with superelastic behavior and radiopacity. This construction has found use in many braided stenting applications, including flow diversion [46]. Variants of DFT wire containing non-concentric cross sections have also been considered but have founded limited commercial use to date [47].

There have been several attempts to use DFT technology to produce optimally-performing absorbable wires [48]. Shaffer et al. investigated FeMn-DFT-Mg composites and found that while they were manufacturable, the Mg cores rapidly corroded once exposed [39]. Griebel et al. experimented with magnesium wires with cores of either pure zinc, pure iron, or other magnesium alloys [49]. These were again found feasible, but the Mg suffered from severe galvanic corrosion when paired with Fe or Zn. Efforts to mitigate the fragmentation risk of FeMn alloys by incorporating a thin filament of a non-degrading metal like nitinol or tantalum proved effective, but full absorption is not achievable with this configuration. On the whole, these efforts have shown the feasibility and potential to modulate degradation sequences of metallic wires but have yet to reach an optimal solution for thin neurovascular scaffolds. The recent introduction of molybdenum (Mo) as an absorbable material option opens a new design paradigm for the thin wires needed for absorbable flow diverters [11,50]. Pairing a shell of FeMnN with one or more Mo cores may provide a wire with good strength and elasticity, a corrosion rate further modifiable by the FeMnN/Mo galvanic pairing, mitigation of fragmentation risk through staged degradation, and good radiopacity from the Mo. Here, we sought to explore and prove the concept of this paradigm through the manufacture and testing of FeMnN-DFT-Mo wires with a variety of cross sections. This small animal pilot study demonstrates the feasibility of manufacturing FeMnN/Mo composites as well as characterizes their in vitro and in vivo corrosion behavior, radiopacity, and mechanical properties.

2. Methods

2.1. Wire manufacturing and material testing

All wire materials used in this study were prepared using conventional cold drawing techniques with single crystal natural drawing dies and mineral oil-based lubricants. Pure Mo wire with a diameter of 1 mm was purchased (Plansee, Reutte, Austria) and drawn to 250 and 80 μm diameters. FeMnN (target composition Fe-35Mn-0.15 N (wt%)) was vacuum induction melted and cast into 50 mm diameter ingots and hot forged to 12.7 mm. From there it was drawn to 250, 80, and 25 μm diameters via a sequence of draw and anneal cycles. The 12.7 mm FeMnN material was also machined into tubes with varying inner and outer diameters for production of FeMnN-DFT-Mo composites followed by similar draw practice to produce testable subcomponents. Composite wires were produced as follows: Wire A had a single Mo core filament which was 60 % of the cross section by area (approximately 67 % by weight). This wire was drawn to 250 μm, 100 μm, and 25 μm diameters. Wire B had 4 individual Mo filaments, each comprising about 1.5 % of the cross-sectional area of the total wire, resulting in approximately 6 % of the cross section being Mo (8 % by weight). One filament was central to the wire and three were evenly distributed around the periphery. This wire was drawn to 250 μm and 100 μm diameters. Wire C was prepared with 15 individual Mo filaments, each consisting of approximately 1.75 % of the cross-sectional area of the wire, for a total Mo content of 26 % by area and 32 % by weight. Wire D had a single Mo core filament which was 20 % of the cross-sectional area (25 % by weight). This wire was drawn to 250 μm and 80 μm diameter. Finally, Wire E consisted of 13 individual Mo wire filaments, 7 of which were 7 % of the cross-sectional area, each, and 6 of which were 1 % of the cross-sectional area, giving a total Mo content of about 55 % by area and 62 % by weight. This wire was drawn to 250 μm and 80 μm diameter. Representative cross sections for wires A-E are shown in Fig. 1.

2.1.1. Tensile testing

Industry-standard tensile testing was conducted for each wire at diameters of 80 μm or 100 μm, at a strain rate of $0.0033s^{-1}$, using a two-column Instron 5569 tensile tester with pneumatic flat face grips at room temperature of 23 ± 3 °C. Strain hardening and associated wire strength were varied with cold work levels for these tensile tested specimens of 90 % (FeMnN, Mo, Wire E, Wire F), 84 % (Wire A, Wire B), or 67 % (Wire C). Cold working by wire drawing is commonly used to simultaneously reduce diameter and increase tensile strength of wire materials [51]. The cold work levels selected here attempted to maximize strength while maintaining manufacturability, which varied by configuration.

2.1.2. Prototype braided flow diverters and radial strength testing

Braided FD's were prototyped out of various wire configurations to establish a proof of concept for manufacturing devices out of the DFT composites and compare the resulting radial strength of devices composed of different materials. The FD's were braided around a 4.75 mm diameter mandrel using 16 individual, 80 μm diameter wires, composed of either pure Mo, FeMnN, or DFT wires D and E. The devices were cut to 2 cm length for radial strength testing. The crush resistance force, defined as the force required to crush the FD to half its initial diameter between two parallel plates normalized to device length, was measured using methods previously described in detail [41,52]. Three replicate devices were measured for each device type.

2.1.3. Radiopacity assessment

To confirm the expected high radiopacity of Mo, a series of 0.075 mm diameter wires of 304V stainless steel, Mo, W, Au, Pt, and Ta were placed onto a 12.7 mm Al plate to serve as a body mimic per ASTM 640. The samples were then imaged on a clinical GE Precision 600 FP imaging system with a Canon DREX-KL80 X-ray generator. Imaging parameters were set to 100 kV and 0.71 mAs. In this imaging mode, higher radiopacity features appear brighter in the image. Grayscale pixel-intensity-difference method was used to quantify radiopacity for three regions of the wire.

To assess radiopacity of the composite FeMnN/Mo wires used in this study, 250 μm diameter specimens were placed onto a 6.35 mm aluminum plate. A Pt/Ta composite wire was used as a reference. Imaging and analysis were conducted as described above. The radiopacity of the braided prototypes described in 2.1.2 were compared with reference to ASTM 640. Additionally, a braid comprising 32 wires of 25 μm Wire A was directly compared to a commercially available flow diverter (FRED; MicroVention, Tustin, California) composed of nitinol and tantalum wires. For this assessment, the braids were imaged with an Artis Zee angiography unit (Siemens, Erlangen, Germany) with a tube voltage of 70 kV. In this imaging mode, higher radiopacity features

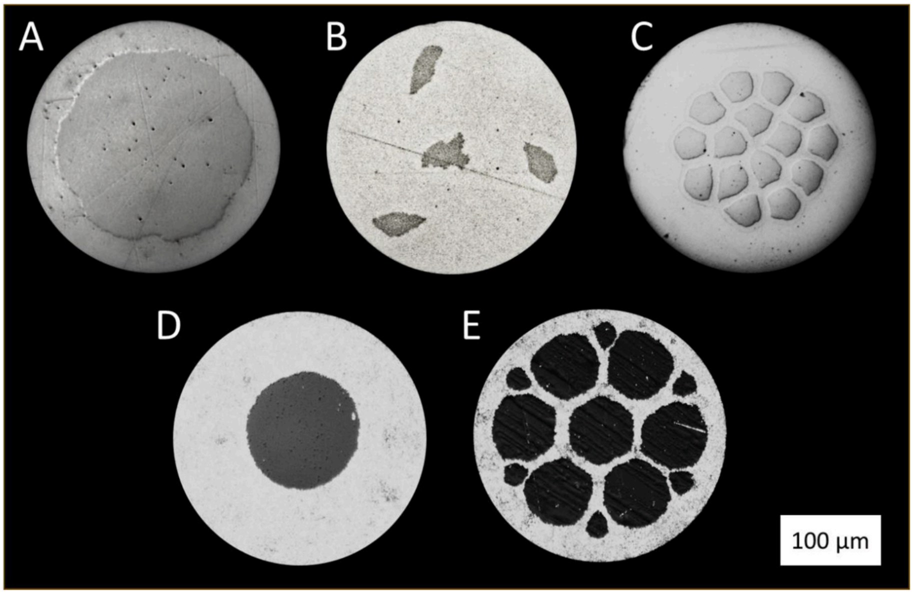

Fig. 1. Representative cross sections of the five composite wires used in this study illustrate versatility of the DFT approach. In these images, the outer shell is FeMnN and the darker filaments are Mo.

appear darker in the image. Five rectangular regions of interest were drawn along the length of each device using ImageJ. The mean greyscale value was recorded for each region of interest.

2.2. *In vitro experimentation*

2.2.1. *Static in vitro corrosion*

Wires 1–2 cm in length from each configuration were cut, and then sanitized in 70 % ethanol before being moved into the laminar-flow hood where they are left for 24 h to evaporate any leftover ethanol. For the B wire imaged for corrosion product identification in Fig. 6., 2 mL of DMEM without FBS was incubated with 1 cm segments between 1 and 5 days and collected every day (5 replicates). For the comparative immersion experiments with wires A, B, and C, approximately 5 mg of wire segments were then incubated with 4 mL of either DMEM (D) or DMEM+FBS (DF) solution for the specified timepoints in six well plate tissue culture dishes. All cell culture fluid and protein solutions were purchased from Sigma-Aldrich. The addition of proteins was performed to test the effect of proteins on corrosion progression. Wires were incubated for 1, 3, and 7 days at 5 % CO_2, 37 °C and a pH of 7.4. Media was removed and changed every 24 h.

2.2.2. *Metallographic preparation and imaging*

Following the in-vitro corrosion experiments, three sections of each sample condition were mounted vertically in epoxy and cut to expose cross-sections perpendicular to the longitudinal axis of the wire. These samples were prepared for optical and scanning electron microscopy following standard mechanical grinding procedures with SiC pads, and subsequent polishing with a water-based alumina suspension to a surface finish of 0.3 μm. Samples were washed thoroughly with ethanol between each grinding and polishing step after 800 grit to prevent contamination or scratching. Optical micrographs of the wires were obtained after polishing using an Olympus PME-3 microscope. Backscattered electron (BSE) images of in vitro tested wires were obtained with a FEI Philips XL 40 Environmental Scanning Electron Microscope (SEM) operating at an accelerating voltage of 20.0 kV and processed with Oxford Aztec software (version 6.1).

2.2.3. *In vitro biocompatibility assessment*

Braids manufactured from FeMnN, Mo, Wire D and Wire E (80 μm wires, 16 wires, 4.75 mm diameter) were subjected to extract mediated cytotoxicity testing, in congruence with the ISO 10993-5 testing standard. The samples were extracted in 1X Eagles Minimal Essential Media supplemented with 10 % fetal calf serum and 2 % antibiotics, at a surface area to volume ratio of 2.08 cm^2/13.5 mL for 24 h at 37 °C. The extracts were PES membrane filtered before cell exposure. L929 fibroblasts were cultured until 80 % confluence and exposed to the extracts in triplicates over 24 h, 48 h, and 72 h incubation periods. Reactivity grades were scored via ISO 10993-5, and 10X images of the monolayers were uploaded to cell pose, where an automated segmenting profile was applied for cell counting. The results are detailed in Supplementary Fig. 1.

2.3. *In vivo implantations*

2.3.1. *In vivo implantations*

All procedures were performed on an IACUC approved protocol at Michigan Technological University. Animals were anesthetized with an isoflurane mixture ranging from 1% to 3%. The surgical site was prepared, and a 100 μm wire ranging from 4 to 8 mm long was implanted into the abdominal aorta of C57Bl/6J (Jackson Laboratories) mice at approximately 12 weeks of age. A detailed account of the implantation procedure can be found here [53]. This approach in both mice and rats has proven to be an efficient and effective method to evaluate biocorrosion of absorbable metals in a vascular environment. Animals were sacrificed at 1 month, 3 months, and 6 months post implantation. The experimental setup is detailed in Fig. 2. Wires corresponding to cross sections A, B and C of Fig. 1 were investigated in vivo.

2.3.2. *Micro CT (μCT)*

To characterize the degradation, the explanted wires were analyzed by computed tomography, using a Bruker Skyscan 2214 nanoscale X-ray computer tomography (μCT) scanner. The scanning parameters for the computed tomography scans were voltage 80 kV, current 150 μA, voxel size ranges from 299 to 380 nm (depending on the straightness of the wire), rotation step 0.2°. The software NRECON was used to transform the longitudinal projection images into transversal sectional images. The analysis software DATAVIEWER was used for slice-by-slice inspection of the transversal images and the analysis software CTVOX was applied for realistic visualization of volumes with different density ranges by 3D rendering.

2.4. *Statistical analysis*

For radial force and radiopacity testing, the data is presented as the mean ± the standard error. All the groups were compared with a one-way ANOVA and a Tukey post hoc test using GraphPad Prism 10, with statistical significance defined as p values less than 0.05. Relationships between radiopacity and alloy density as well as molybdenum area percentages were determined using linear regression in Minitab 20.

3. Results

3.1. *FeMnN-DFT-Mo composite material characterization*

The tensile curves of each material configuration presented in Fig. 1 are shown in Fig. 3A. Table 1 shows the tabulated values from stress strain curves, performed in triplicate. The FeMnN and Mo wires possess approximately similar UTS (1945 ± 26 vs 1998 ± 1 MPa) and overall elongation (3.0 ± 0.4 vs 2.7 ± 0.2). There is a significant difference in modulus between FeMnN and Mo wires (162 ± 0.5 vs. 272 ± 4). Wire A displays slightly larger elongation compared to both Mo and FeMnN, yet an overall lower UTS. Wires B and C are less ductile and less strong when compared to FeMnN and Mo. Wires D and E show properties that are largely similar to FeMnN and Mo. Wires A and E show increased modulus above that of FeMnN (Table 1).

The crush resistance force of braided FD prototypes composed of wires of pure Mo, FeMnN, and DFT wires D and E are presented in Fig. 3B. One of the pure Mo replicates was an outlier due to an error with the linear motion stage and was therefore omitted. The pure Mo devices exhibited the highest mean crush resistance force, and the FeMnN device had the lowest. The means of the two DFT configurations fell within the range of the FeMnN and Mo. The ANOVA was statistically significant, with a p value of 0.0002. When comparing individual groups, there was a statistically significant difference between all devices except the pure Mo and DFT Wire E. Generally, increased Mo content in the wires corresponded to a higher crush resistance force of the braided FD's.

An x-ray image of Ø75 μm Mo compared to stainless steel and other radiopaque materials is shown in Fig. 4A. The grayscale value of the Mo (29.3 ± 1.5) was four times that of 304V (7.3 ± 1.5) and 60–73 % that of W (43.3 ± 2.1), Au (44.7 ± 6.1), Pt (48.7 ± 6.0), and Ta (40.0 ± 2.6). Statistical significance between these groups is shown in Fig. 4B. All the materials were significantly more radiopaque than 304V. There was no statistical difference between W, Au, Pt, and Ta. However, all these materials were significantly more radiopaque than Mo. Radiopacity in relation to material density is shown in Fig. 4C. An x-ray image of Ø250 μm FeMnN and Mo monofilament wires and their DFT counterparts are shown in Fig. 4D. Resulting grayscale values and their significance are shown in Fig. 4E. The radiopacity was significantly different between all groups, other than Mo and Pt/Ta; and wire A and wire E. FeMnN (120 ± 2) is substantially less radiopaque than Mo (232 ± 1), which approaches the Pt/Ta composite (234 ± 1) in terms of radiopacity. Incorporation of

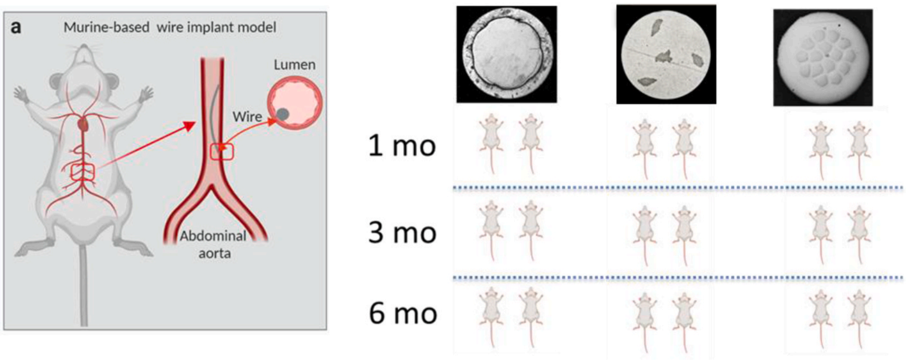

Fig. 2. Summary of in vivo experiments.

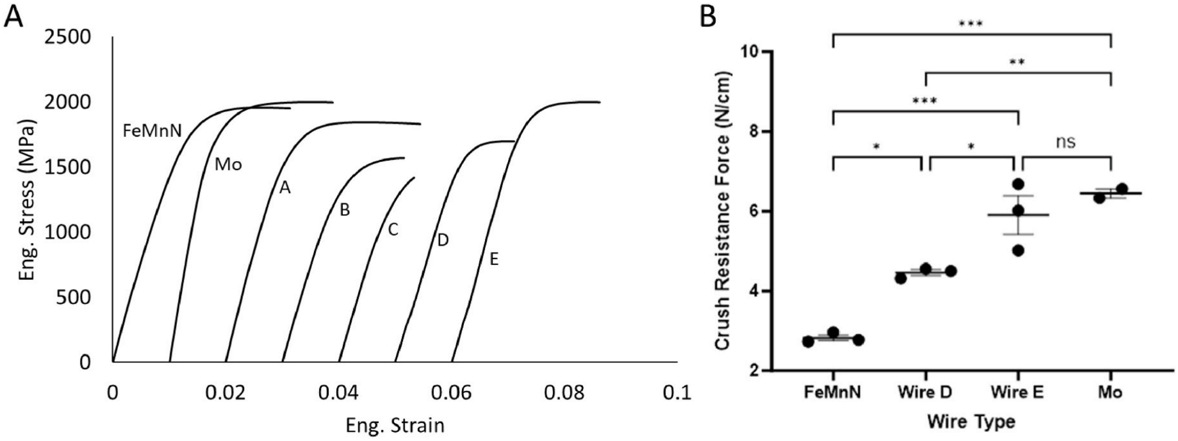

Fig. 3. A) Stress-strain curves of composite wires, compared to FeMnN and Mo. **B)** Crush resistance force of braided FD's composed of FeMnN, Mo, or DFT configuration D and E wires. $^{*}p < 0.05$, $^{**}p < 0.01$, $^{***}p < 0.001$.

Table 1
Summary of mechanical properties from each DFT configuration, performed in triplicate.

		UTS (MPa)	YS (MPa)	Elongation (%)	E (GPa)
FeMnN	avg	1945	1623	3.0	162
	stdev	25.79	33.82	0.4	0.50
Mo	avg	1998	1701	2.7	272
	stdev	0.95	25.45	0.2	3.95
Wire A	avg	1859	1595	3.5	167
	stdev	1.30	16.24	0.1	10.15
Wire B	avg	1516	1277	2.1	146
	stdev	20.51	27.90	0.1	2.59
Wire C	avg	1255	1090	1.1	155
	stdev	24.38	15.87	0.2	5.49
Wire D	avg	1694	1603	2.1	148
	stdev	5.44	11.67	0.0	1.69
Wire E	avg	1996	1840	2.7	169
	stdev	6.89	9.44	0.1	3.04

Mo filaments into the FeMnN shell greatly enhances radiopacity, in proportion to the amount of Mo in the cross-section (Fig. 4E and F).

Imaging of the braids provided further confirmation of the radiopacity enhancement offered by the Mo over FeMnN. The radiopacity of a 32-wire Ø25 μm Wire A braid was comparable to FRED, a commercially available flow diverter (Fig. 5A and B). The majority of the radiopacity in FRED was imparted by several tantalum wires incorporated into a braid primarily of nitinol wires, whereas the DFT braid had a much more uniform radiopacity [54]. The 16-wire Ø80 μm braids (Fig. 5C) showed increasing radiopacity with increasing Mo content (Fig. 5D). These results demonstrate that both device radial strength and radiopacity can be improved by increasing the Mo content in FeMnN-DFT-Mo wires.

3.2. *In vitro corrosion behavior and cytotoxicity*

We sought to evaluate the general corrosion behavior of the selected DFT composite configurations in vitro using a static culture immersion approach. Our conditions reflect DMEM fluid with and without proteins ("DF" and "D" respectively). Fig. 6 displays selected cross sections from these experiments, with the upper three rows of images taken with optical microscopy and lower three rows of images taken with SEM-BSE. During preparation, polishing artifacts were routinely seen resulting in etching like presentation for the optical microscopy group of images. This effect is significantly reduced when visualizing the materials with SEM-BSE due to the deeper origin depth of backscattered electrons within the interaction volume. Generally, we observed a substantial increase in corrosion activity upon the addition of proteins for all three materials. This trend is best exemplified by the 7-day timepoints in Fig. 6. When comparing D1 to DF1 at 7 days, significant material loss is seen in the DF1 group when compared to D1. The same trend is seen for D2 vs. DF2, and D3 vs. DF3 at 7 days (Fig. 6). The cross-sectional micrographs reveal cracks with the FeMnN alloy after in vitro corrosion, most pronounced in the Wire B propagating with a similar central crack to the middle Mo filament, but also in the Wire C growing towards the middle in between the 15 Mo filaments. Based on the setup of the DFT wires, the crack in the Wire A is the shortest by being stopped at the Mo filament.

Cells were rated on their qualitative appearance at 72 h according to a reactivity grading scale (0–4, with 0 marking no cytotoxicity and 4 marking severe cytotoxicity) given in ISO10993-5. Representative

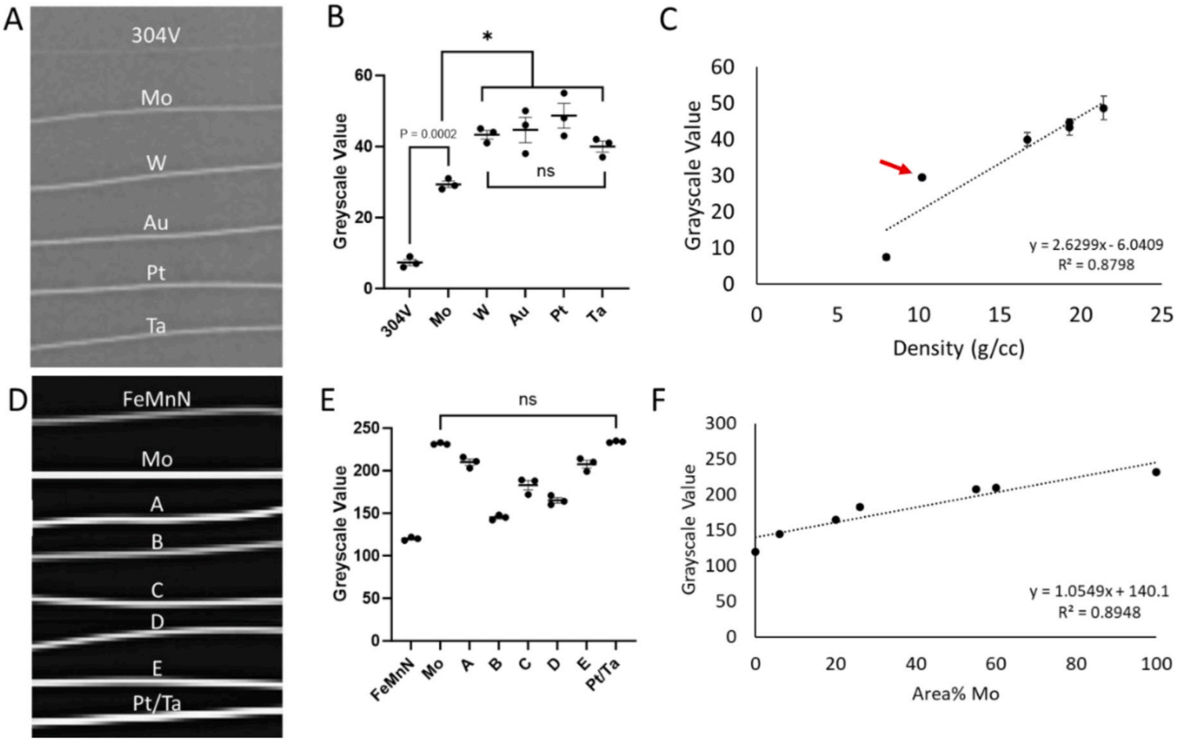

Fig. 4. A) X-ray image of Ø75 μm Mo compared to stainless steel and other radiopaque materials. **B)** Grayscale intensity values and statistical significance of the wires in A. **C)** Grayscale values in relation to density, a key factor in radiopacity. Notably, Mo (red arrow) is above the trendline. **D)** X-ray image of Ø250 μm wires used in this study, with a Pt-Ta composite for reference. **E)** Grayscale intensity values and statistical significance of the wires in D. **F)** Grayscale values in relation to the percentage of each wire's Mo proportion.

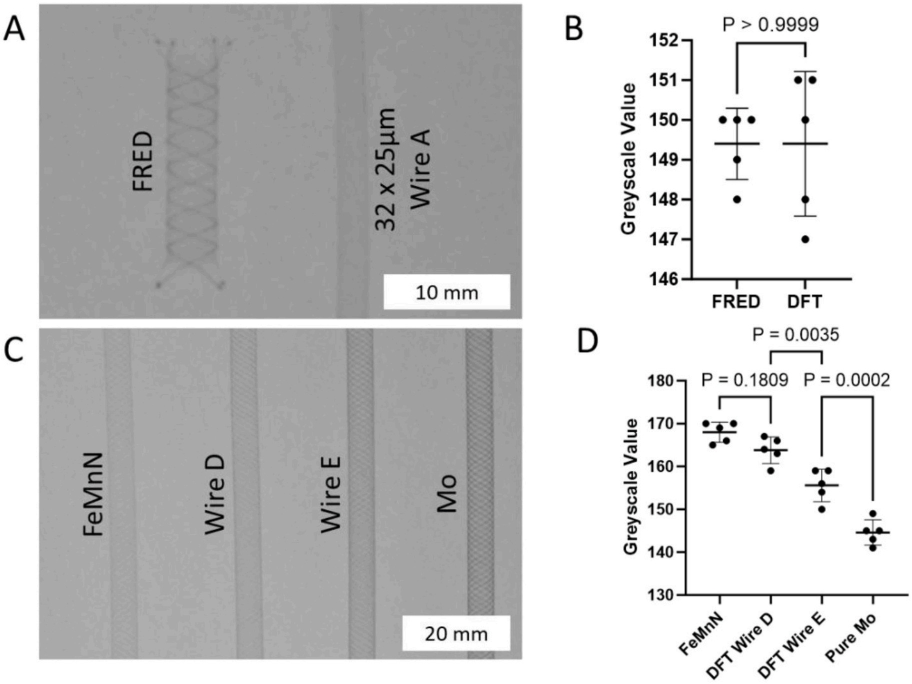

Fig. 5. A) Radiograph of commercial flow diverter (FRED) compared to a 32-wire braid of Ø25 μm Wire A. **B)** Grayscale values of regions of the stents shown in A. C) Radiograph of 16-wire braids of Ø80 μm wires of FeMnN, Wire D, Wire E, and Mo. **D)** Grayscale values of regions of the stents shown in C.

images of the cell monolayers can be found in Supplementary Fig. 1. The positive control displayed severe cytotoxicity, with all replicates receiving a 4 ± 0 rating. FeMnN, and Mo braids displayed no overt qualitative cytotoxicity and were both graded 0, while extracts from braids of wire D and wire E were graded at 0.7 ± 0.6 and 1 ± 0 respectively, suggesting slight cytotoxicity. Cells were counted from 3 representative fields of view of each replicate and presented in Supplementary Fig. 1. When tested by one way ANOVA, the dataset was not

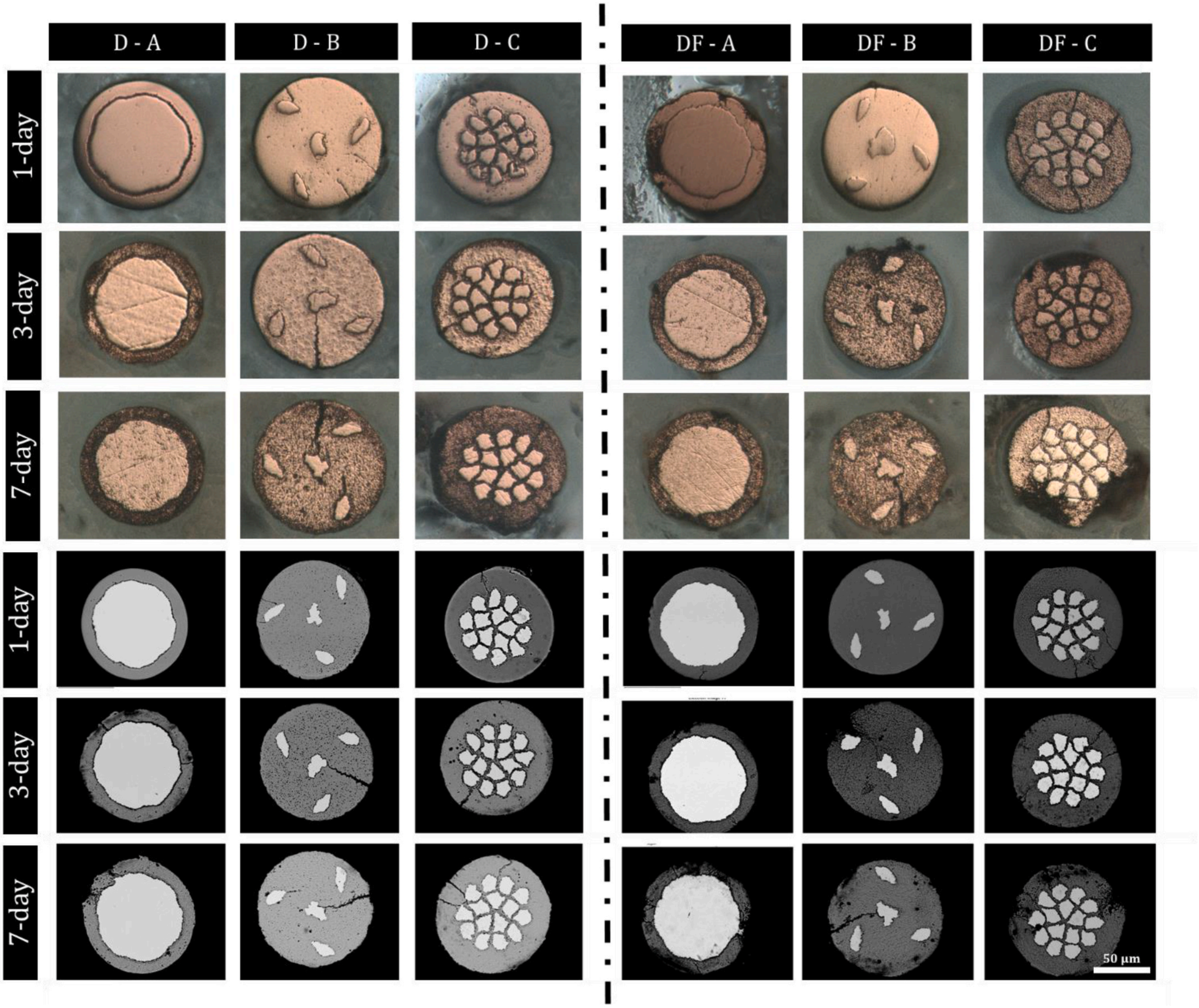

Fig. 6. In vitro corrosion analysis of the three DFT wires with Wire A, Wire B and Wire C filaments after corrosion over 1, 3, and 7 days. The upper three rows of images are taken with optical microscopy and lower three rows of images are taken with SEM-BSE. Scale bar is 50 μm.

significant. When compared to the negative control at 48 h (97 ± 102 cells/mm^2), there appears to be a slight reduction in cell number for the FeMnN, wire D, and wire E conditions (15 ± 4, 41 ± 4, and 5.9 ± 2.6 cells/mm^2 respectively), although this reduction in cell number is not statistically significant. By the 72 h mark, extracts from FeMnN, Mo, wire D and wire E (106 ± 76, 190 ± 156, 99 ± 35 & 86 ± 86 cells/mm^2 respectively) appear to have minimal impact on cell number when compared to the negative control (133 ± 131 cells/mm^2), which is in congruence with the qualitative assessment on cellular appearance via the reactivity scale.

3.2.1. *Corrosion product characterization*

After evaluating all conditions, we selected cross sections that contained the most voluminous product, which were found at 1- and 5-day static immersion in the non-protein containing solution for Wire B, to evaluate corrosion products. There was significant Mo Lα overlap with P and Cl and should not be interpreted as positive element presence in the filaments in both scans of Fig. 7. At day 1 (Fig. 7A), the corrosion product contains Fe, Mn, O, dispersed throughout the entire product. Interestingly, there is a Mn rich outer product that is not contiguous along the formed oxide, which is seemingly low in Fe. Ca and P are found predominately on the outer edge of the oxide that contacts the fluid. Cl can be seen within the product layer, although not distributed homogenously throughout. Significant changes in the corrosion product distribution of elements are seen when evaluating the 5-day sample presented in Fig. 7B. In some regions at the interface, Mn rich areas can be seen sporadically, which do not appear to stoichiometrically match Fe content. Based on O counts, oxide regions deeper within the wire cross section (closer to the central Mo filament) contain less O when compared to the regions that are closer to the fluid interface. Additionally, the Ca and P maps are not in complete agreeance of localization at the fluid interface, suggesting another P containing species that is present other than a calcium-phosphate product. The Cl distribution appears to localize heavily at the metal-oxide interface, suggesting localized metal attack by Cl ions and an active metal interface that is not yet passivated.

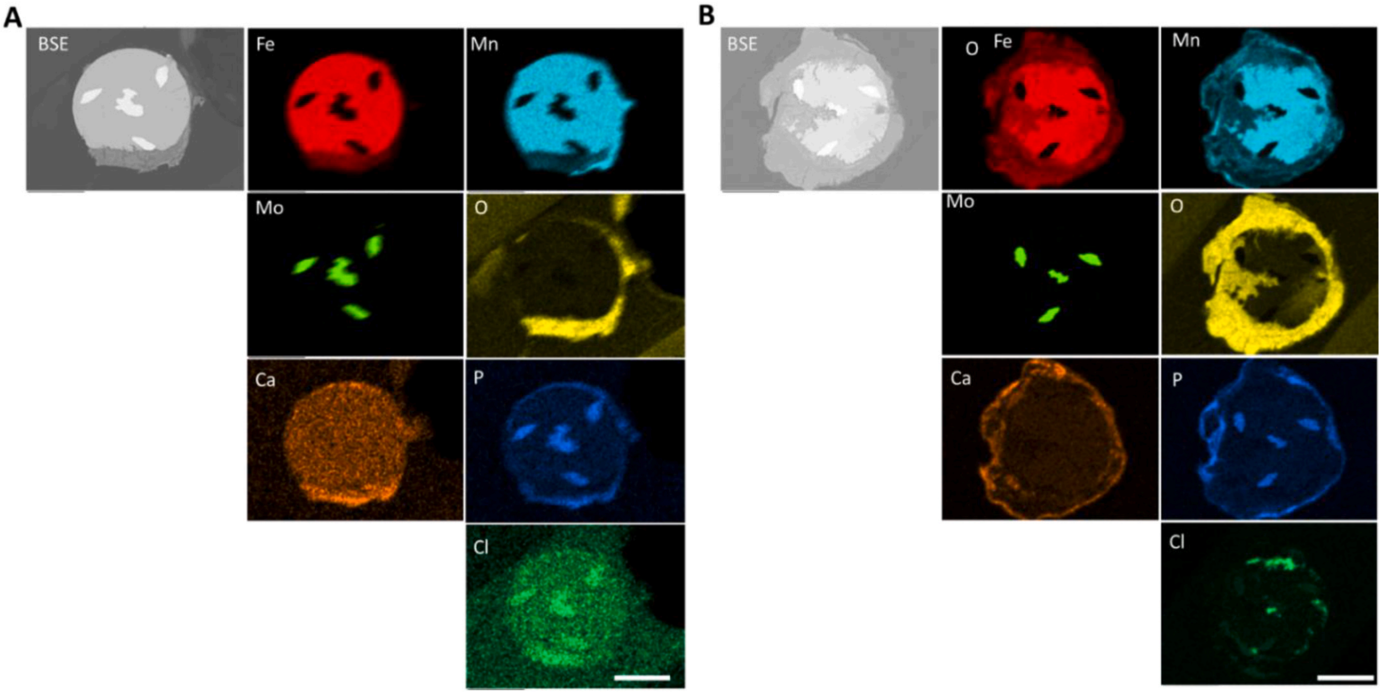

Fig. 7. Corrosion product analysis on in vitro static corrosion tests for wire B in DMEM **A)** Wire B SEM-BSE and EDS maps at 1 day corrosion and **B)** at 5 day corrosion. Scale bar is 50 μm.

3.3. In vivo corrosion performance

3.3.1. Macroscopic evaluation

Upon collection, wires were observed for general corrosion in situ. The arterial wall of the mouse aorta is thin (100–150 μm approximately), and relatively transparent, allowing visualization into the lumen with appropriate lighting. Results are outlined in Fig. 8. The anchoring silk sutures are shown in yellow when visible. Between the yellow arrowheads the wires experience the luminal blood flow environment, while the regions outside the arrow heads denote the wire in the adventitia of the artery. At 1 month, most of the corrosion activity appears to take place in the adventitial region of the wire, with minimum activity within the lumen. At 3 months, Wires A and B experience progression of corrosion within the lumen space, while Wire C shows minimal progression within the lumen. At 6 months, there is significant corrosion activity for all three wires, with activity in the lumen, and

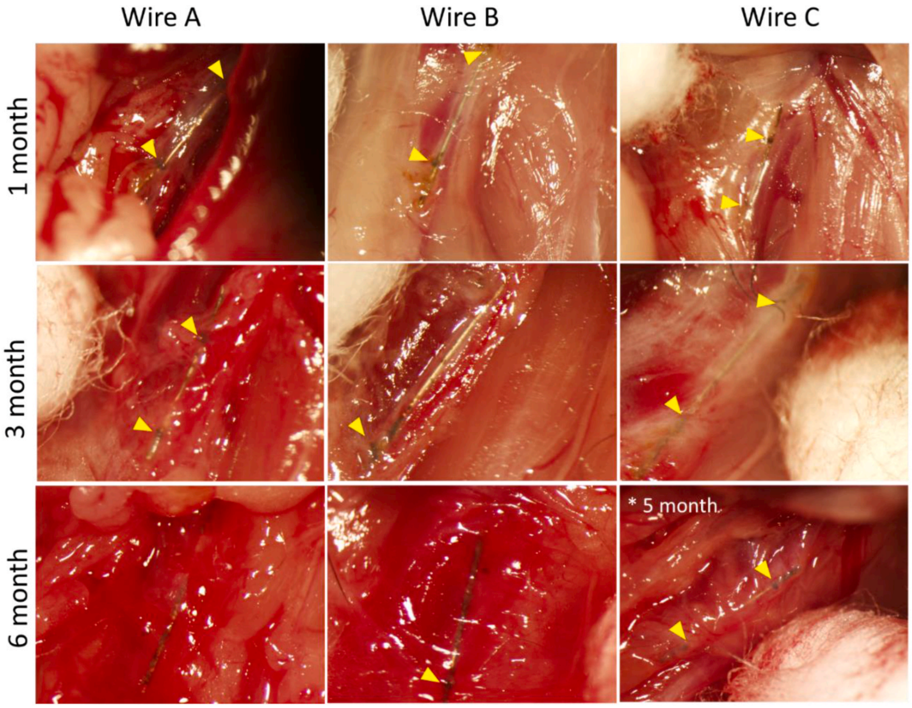

Fig. 8. Macroscopic view of DFT implants within the abdominal aorta of mice at each implanted timepoint. Yellow arrows show suture points anchoring the wire within the vessel wall. Wire C is shown at 5 months instead of 6 months implantation.

adventitial segments of the artery.

The progression of corrosion with time can also be seen from the 3D-reconstructed μCT images, see Figs. 9A and 10A. The Mo filaments, having a very high density, present themselves in white, with less dense FeMnN regions in gray, and the even less dense corroded regions in dark gray to black. The images reveal local corrosion, but no critical corrosion pits were found when compared with other Fe alloys [55].The 2D- μCT scans of the DFT wires degraded in vivo show surface and sub-surface corrosion (Fig. 9B). Wire A shows strong interfacial corrosion between the FeMnN material and the Mo core filament, acting as the cathode in the DFT wire. Surprisingly, after 6 months the Mo core filaments do not show any signs of corrosion attack. Wire B is the only wire configuration which gives evidence of cracks during in vivo corrosion (Fig. 9A and B and 10A). At 6 months, wire B reveals a crack all along the wires length and connects all the corroded areas. The sub-surface corrosion, seen mostly after 3 months, is developing completely along the FeMnN material including the surface. Also, wire C underlines the cathodic effect of the Mo filaments, with the FeMnN material is corroding in between the Mo filaments (Figs. 9A and 10A). Metallographic cross-sections, not shown here, did not reveal cracked FeMnN material. The SEM-EDS mapping of wire B from a 6-month implanted sample in Fig. 10B shows in agreement to the in vitro results, see Fig. 7B, that oxide regions (see O counts) reach deeper in the wire cross section towards the central Mo filament. The inner corroded areas contain less O when compared to the regions that are closer to the fluid interface.

4. Discussion

The concept of absorbable FD's has been previously proven feasible in animal models using polymer-based scaffolds [13,19,21]. Critically,

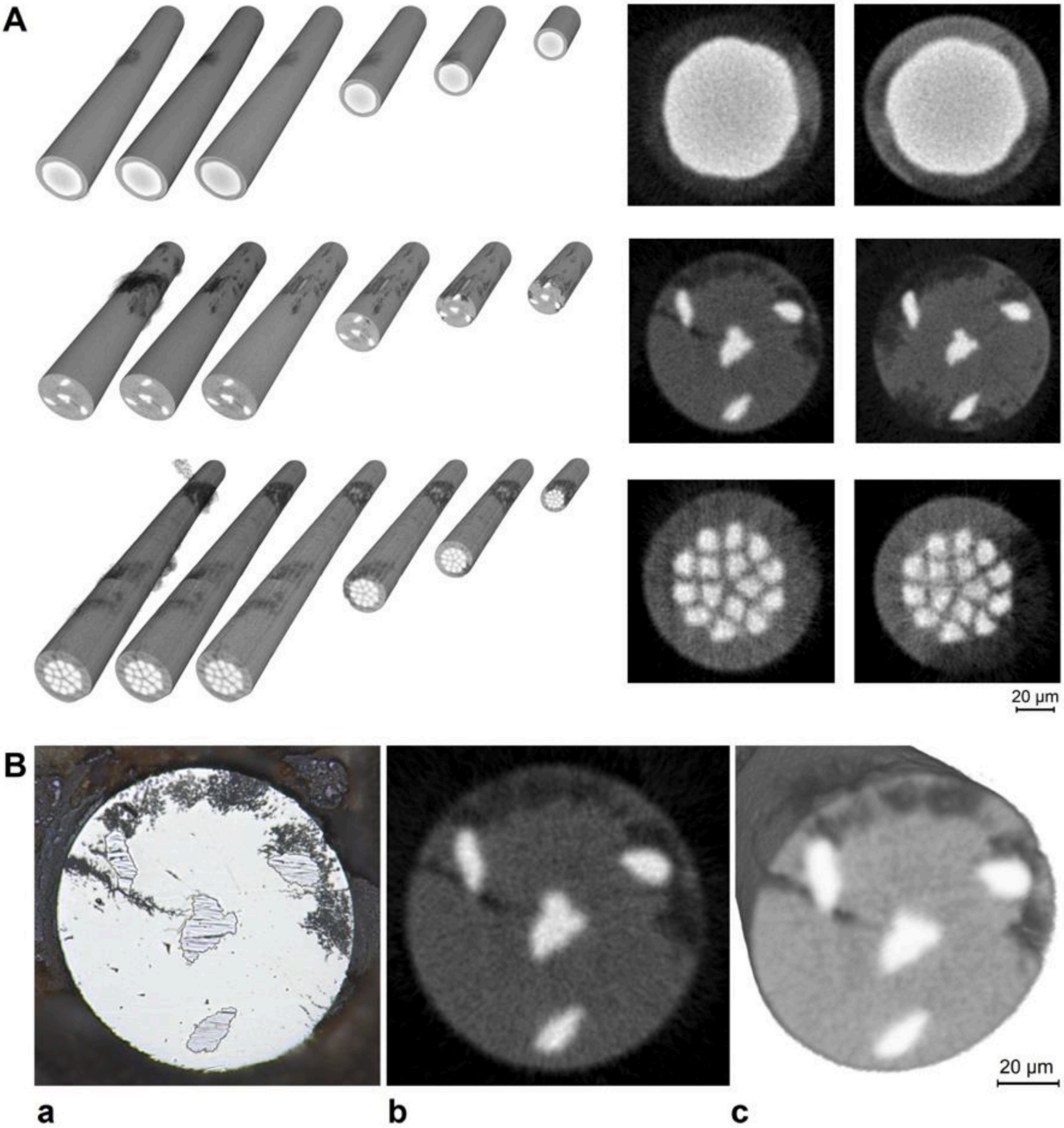

Fig. 9. A) Representative 3D-reconstructed images and 2D μCT of DFT wires A, B, and C after implantation over 3 months. 3D image from left to right: reducing the amount of tissue/product grown onto and into the degradation layer and second cutting further through the wire to reveal additionally cross-sections, 2D scans randomly chosen at degraded parts, wire diameter 100 μm and length up to 1 mm **B)** Cross-sectional micrograph of wire B, degraded over 3-month, a) metallographic cross-section by light microscopy, b) μCT -scans and c) 3D-reconstructed image.

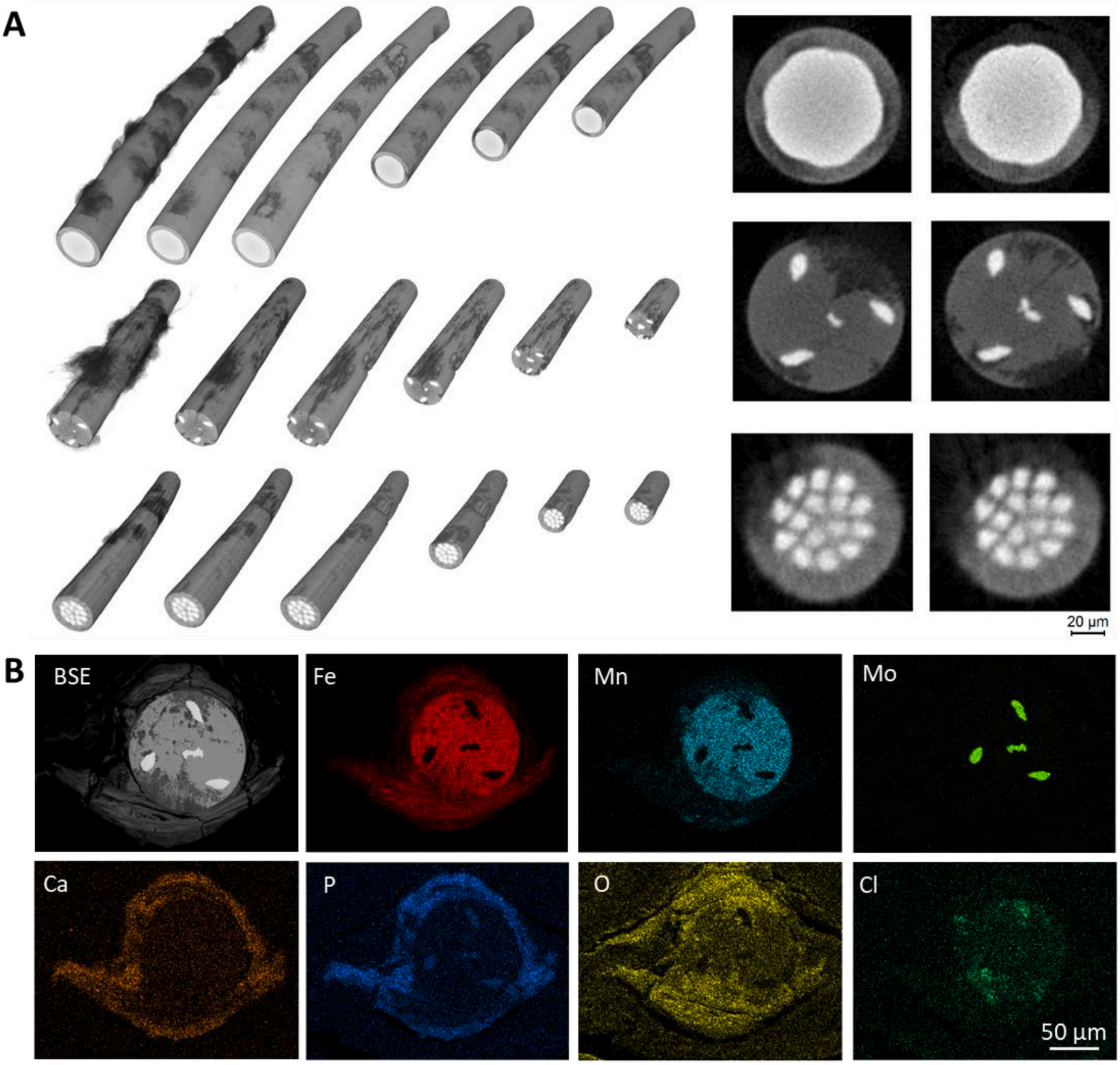

Fig. 10. **A)** Representative 3D-reconstructed images (left) and 2D-nanoCT-scans (right) of wires- A (top), B (middle), and C (bottom) after implantation for 6 months. In the 3D images from left to right, the visible contrast limits are modulated to reduce the amount of visible tissue grown onto and into the degradation layer and to reveal additional cross-sections. 2D scans were selected to highlight typical degradation maxima. **B)** SEM-EDS mapping of wire B from a 6-month implanted sample. In all cases, wire diameter is 100 µm.

these devices present challenges that are difficult to overcome with polymer material systems. The overall lower modulus and elasticity of polymers when compared to metal materials generally requires that devices fabricated from standard polymers to have larger strut dimensions to compensate (≥40 µm), or in some cases incorporate permanent metal wires within the braid to bolster device radial strength and self-expandability [13,19,21]. It should be mentioned however that flow diverters require lower radial strength requirements when compared to balloon expandable stents, which allows some polymer configurations to achieve success [14]. Regardless, absorbable metals such as Fe and Mo could provide increased strength, modulus, elasticity, and radiopacity at current state of the art flow diverter dimensions when compared to bioabsorbable polymer systems. In this work, a variety of composite wires with FeMnN alloy shells and one or more Mo cores (Fig. 1) were successfully manufactured and assessed for suitability as an absorbable flow diverter material.

4.1. Mechanical properties

In 2012, Schaffer et al. demonstrated that Fe35Mn alloys could exhibit greater than 1 % elastic strain and yield strengths >1 GPa [39]. We recently performed benchtop evaluations of FeMnN based flow diverters prototyped with individual wire diameters and an overall wire count comparable to FDA approved FD's [41]. We found they exhibited crush resistance values that met current FDA-approved FD's. Motivated by these findings, we evaluated FeMnN alloy for use in our DFT composites. The FeMnN displayed high yield strengths and a large range of elastic deformation, which is ideal for a self-expanding material. Our reported modulus values for FeMnN are slightly lower than currently used CoNiCr alloys, which would result in lower comparative radial force values but allows for greater elasticity for equivalent yield strengths. The higher modulus of Mo may limit elasticity but does confer good radial force. Employing the DFT wire compositing approach with FeMnN and Mo allows for tuning of the overall mechanical properties by varying the relative amounts and positions of each material in the cross-section, as demonstrated in Fig. 3A and Table 1. It is important to note that the primary deformation mode of wires in a braided FD is bending. In bending, the material near the surface (furthest from the neutral axis) experiences the highest strains and dominates the overall wire response. In these configurations, the FeMnN shell provides a relatively high elastic response during initial deployment. Use of a tensile test to measure the elastic modulus weights all parts of the cross-section equally and does not account for the strain gradient in bending. Wires A and E both possessed tensile moduli higher than that of FeMnN, although with some variability which we speculate are due to manufacturing inconsistencies. Additionally, other wire geometries demonstrate some mechanical penalties when compared to the non-DFT forms. In Fig. 3B we demonstrated that devices prototyped out of DFT wires had a higher radial strength than FeMnN wires, with higher radial strength trending with increasing Mo content. One drawback of the experimental design presented here is the inability to fully recapitulate the complex loading that happens during deployment and long-term residence in vivo. Future work should attempt to describe the relationship between the DFT geometric configuration and mechanical performance both during deployment and in various stages of degradation in more realistic situations.

4.2. Radiopacity

The first absorbable FD attempts with polymers are plagued with the lack of radiopacity, due to the low atomic number and density of polymers. Innovative strategies to enhance radiopacity include $BaSO_4$ coatings and mixing polymer melts with other radiopaque materials work to some extent [20,56]. Ultimately, Jamshidi et al. and Sasaki et al. included tantalum coated nitinol wires within the braid or, gold markers at the device ends, respectively, to increase radiopacity for their engineered FD's, negating full absorbability [13,19]. The high atomic number and material density of Mo in relation to other absorbable metals will theoretically result in enhanced radiopacity. In this work, we have extensively characterized and confirmed this effect. X-ray imaging of Ø75 μm wires of stainless steel, Mo, W, Au, Pt, and Ta showed that while Mo was not as radiopaque as a material like Pt, it is not far off from Ta and provides dramatically better visibility than stainless steel (Fig. 4A and B). The incorporation of Mo into FeMnN using the DFT approach enables dramatic enhancements in visibility over a solid FeMnN wire (Fig. 4D and E), and this effect holds in proportion to the amount of Mo in the composite (Fig. 4F). This effect was further confirmed through testing of wire braids, a geometrical structure approximating actual flow diverter devices. Fig. 5A shows an x-ray of a simple 32-wire braid of Wire A where each wire is 25 μm in diameter, appropriate for flow diversion devices. Adjacent to this braid is a commercial flow diverter comprising many wires of nitinol as well as some tantalum wires for added visibility. Though the Wire A braid is not as intensely visible as the Ta marker wires in the FRED device, there is no significant difference between the two constructions, suggesting that a flow diverter using a Wire A type cross-section would have sufficient radiopacity to enable accurate device placement. While DFT technology is utilized in FDA approved neurovascular scaffolds to increase radiopacity with a platinum core, to the authors' knowledge this is the first instance of a DFT based wire material that concomitantly increases radiopacity while maintaining full absorbability.

4.3. Corrosion behavior of FeMnN-DFT-Mo wires

Generally, the overall corrosion morphology was similar with and without proteins. The obvious differences are the concentration of cracks, and the degree of corrosion activity. The addition of proteins to DMEM increases the corrosion activity for all three materials. For biodegradable Mg alloys, the corrosion rate decreases with increasing the complexity of the medium components [57]. Here, we document an opposite phenomenon regarding protein interactions when compared to Mg. This behavior for Fe-Mn alloys has been observed in other in vitro studies [58]. While the exact mechanism of corrosion interaction with proteins for Fe-Mn materials is currently unclear, the presence of proteins shows yet another dimension of changes in fluid biochemistry interacting with the metal surfaces.

By 7 days of immersion, the activity of corrosion throughout the cross section of the composite materials is highly apparent for all configurations. Additionally, the presence of Cl at the metal oxide interface of the 5 day immersion sample presented in Fig. 7 suggests a non-passivating corrosion product layer, that is easily penetrable by aggressive Cl anions [55]. It is interesting that we generally do not observe large voluminous product accumulation which is seen with Fe materials in vitro (Fig. 6). We also do not see large accumulations of product in vivo throughout our experiments. (Figs. 9 and 10). A straightforward explanation could be the result of using the Fe35Mn system, which possess a 35 % by weight reduction of Fe material which would be available to form products. In vivo investigations of Fe to date generally use pure Fe materials that have been nitrided with a small amount of nitrogen comprising its total weight. An alternative explanation could be directly due to the sacrificial anode pairing of FeMnN with Mo. Through currently unknown reaction cascades, it could be possible that more soluble Fe species are produced than insoluble products. More detailed corrosion studies would need to confirm this progression and interrogate corrosion products with quantitative vibrational spectroscopies.

Our 3 month and 6-month implants show an increase in corrosion activity via μCT. In agreement with the literature, the in vivo corrosion is much slower than in vitro, with 5 days in vitro in DMEM approximating the same volume loss as in 3 and 6 month in vivo (Figs. 9B and 10). It is expected that the Mo filaments do not corrode as long as there is less noble FeMnN material acting as an anode in these composite fine wires. Otherwise stated, as long as the more corrosion-active FeMnN species is locally available, the more noble Mo structure is preserved, thereby acting to delay strut failure events. The different DFT approaches will behave differently, as example, tissue can grow in between the Mo filaments and stabilize the composite wire under degradation in Wire B and Wire C. We did not observe any corrosion of Mo for any of the conditions investigated. Mo is known for degrading with a very uniform degradation layer [50] and we do not expect deviation from previously observed degradation morphology in these configurations. In fact, this expected uniform degradation paired with the demonstrated delay in Mo degradation suggests that these composites will likely resist premature fracture of the bulk wires.

We present a corrosion progression scheme for the generalized FeMnN/Mo pairing in Fig. 11. Upon initial contact with the physiological fluid, local coupling along the interface of the two materials initiates the corrosion reaction. As electrons flow from the less cathodic FeMnN material, the cathodic reaction proceeds on the Mo filament and iron ions are liberated from the anode. This local reaction continues and causes corrosion of the interface, which is seen for wire configuration A in Fig. 9. We see buildup of corrosion product as the corrosion reaction continues, which from our qualitative experiments does not inhibit progression of corrosion (Fig. 9.) We believe this is directly due to the distant coupling that happens along the length of the wire, which should theoretically continue until all FeMnN has lost electrical contact. When full degradation of the anodic FeMnN takes place, the Mo filaments should begin degrading similarly to mechanisms outlined in literature [50,59].

4.4. Biocompatibility

Fe materials have demonstrated acceptable biocompatibility for use in the vascular system historically [30–34,60]. Initial reports using pure Fe demonstrated the slow of clearance of insoluble Fe products, with moderate inflammatory responses directed towards the stable oxides and phosphates [31,32,60]. Currently, the base of Biotyx Medical's IBS scaffold consists of a plasma nitrided pure Fe, which successfully increases the corrosion rate of the material which experiences >95 % absorption at 13 months in rabbit abdominal aorta's [30,33,34]. With this increase in corrosion, minimal lumen loss and neointimal hyperplasia were observed. The authors suspect the product is concentrated in

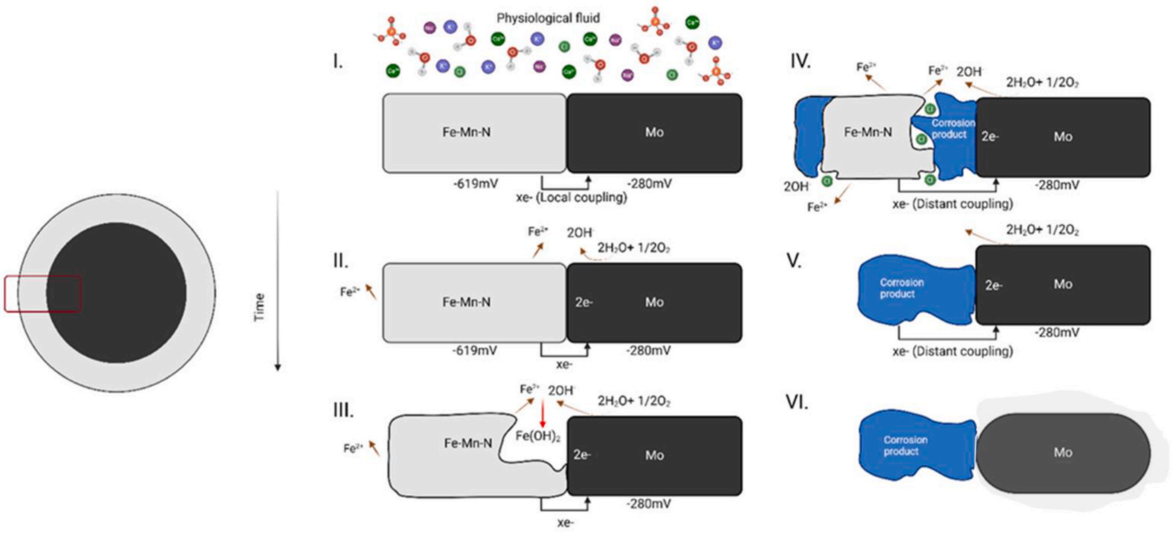

Fig. 11. Corrosion progression mechanism of FeMnN-DFT-Mo wires.

macrophages and precipitated with hemosiderin, and successfully cleared through draining arterial lymph nodes. We observed a Fe product cloud that appeared to be biologically transported away from the implant site for multiple DFT wires at 3 and 6 months, which corroborates with the purported clearance mechanism of Fe materials (data not shown). Additionally, the endothelial favorability of Fe35Mn has been demonstrated in vitro [61].

We have performed extract-based cytotoxicity testing on FeMnN, Mo, Wire E and Wire D braids in vitro (Supplementary Fig. 1). No statistical differences were noted in cell density when tested by one-way ANOVA. There were however slightly (non-significant) reduced cell numbers at the 48 h mark for FeMnN, Wire D, and Wire E conditions when compared to controls. This may suggest a slight impairment on the proliferation rate by the FeMnN material extract, however cell numbers were recovered at the 72 h mark to levels similar of the control condition. It is interesting that the pure Mo extract did not impart a similar trend in reduction of the proliferation rate at 48 h. Furthermore, the cell density at 72 h was highest for Mo on average compared to any of the conditions tested. These preliminary results may hint at beneficial effect of Mo products on L929 proliferation, although rigorously designed experiments should be performed to determine the effective concentration range that would elicit this effect. Fe ions have been previously shown to reduce cellular proliferation and modulate gene expression [62], therefore the reduction in growth rate of L929 cells when cultured with an FeMnN based extract is not surprising. Although the apparent growth rate appeared to be slightly reduced, no major qualitative changes were observed in cellular morphology for any of the stent extract conditions, indicating acceptable cytotoxicity.

Mo is a relatively new biomaterial, which was introduced in 2019 and subsequent preclinical animal experiments performed shortly thereafter [11,50,63]. Initial in vitro experiments demonstrated that MoO_4^{2-} could possibly exhibit differential toxicity towards endothelial cells, when compared with smooth muscle cells [59]. Sikora et al. evaluated pure Mo wires at 6 months in healthy C57 mice using the aorta wire model, and evaluated tissue sections for smooth muscle cell content, endothelial cells, and macrophages. The authors found that CD31 expression on the Mo containing neointimas, corresponding to endothelial cell coverage, was lower when compared to Pt controls [50]. There was no observation of progressive inflammation or smooth muscle cell toxicity. While this phenomenon should be further investigated, the application of Mo in the DFT configuration offers some benefits regarding biocompatibility. The overall amount of Mo used is lower due to its fractional cross-sectional presence in the geometry, and the migrating endothelial cells are largely protected by the outer FeMnN shell from Mo. Further, Mo degradation theoretically will not begin until the sacrificial anode effect of the shell is diminished, which should allow for appropriate endothelial bridging and neointimal tissue healing. We have not seen degradation of any of the Mo filaments in any of the in vitro or in vivo studies. We speculate the staged degradation would allow for the neointima to mature and fully reendothelialize, with local inflammatory cells experiencing the highest amount of Mo by the time degradation commences. In our current 100 μm FeMnN-DFT-Mo composites, Mo degradation would not commence within the first 6 months (Fig. 10), which could act as a stable endothelial bridge across aneurysm necks to allow robust healing. Future work should extend past the FeMnN degradation phase and analyze late stage Mo corrosion.

5. Conclusions

In this small animal pilot study, we can conclude the following:

1. The DFT approach with Mo as a core material can be used to increase radiopacity of FeMnN wires as fine as 25 μm.
2. Mo core(s) can provide mechanical tuning to FeMnN wires, providing higher crush resistance of FeMnN-DFT-Mo stents.
3. In vitro corrosion of FeMnN-DFT-Mo composites is sensitive to corrosion media parameters such as protein content.
4. FeMnN-DFT-Mo wires demonstrate absorbability at six months in mouse aortas, with FeMnN acting as the sacrificial anode.
5. Mo corrosion has not been observed at 6 months in vivo, indicating galvanic pairing can prevent premature wire fragmentation.

Declaration of competing interest

Adam Griebel and Jeremy Schaffer are employees of Fort Wayne Metals.

Ramanathan Kadirvel: ownership in Monarch Biosciences; and support of non–study-related clinical or research effort overseen by the author from Cerenovus Inc., Medtronic, Endovascular Engineer-ing, Frontier Bio, Neurogami Medical, MIVI Biosciences, Monarch Biosciences, and Stryker Inc.

David Kallmes: ownership in Conway Medical, Piraeus Medical, Nested Knowledge, and Superior Medical Experts; and support of non–study-related clinical or research effort overseen by the author from Medtronic, MicroVention, Monarch Biosciences, Balt, Cerenovus, and Stryker.

Ethics approval and consent to participate

All procedures were performed on an IACUC approved protocol at Michigan Technological University.

CRediT authorship contribution statement

Adam J. Griebel: Writing – review & editing, Writing – original draft, Supervision, Project administration, Methodology, Investigation, Formal analysis, Data curation, Conceptualization. **Petra Maier:** Writing – original draft, Visualization, Supervision, Methodology, Data curation, Conceptualization. **Henry Summers:** Writing – review & editing, Data curation. **Benjamin Clausius:** Writing – original draft, Formal analysis, Data curation. **Isabella Kanasty:** Data curation. **Weilue He:** Data curation. **Nicholas Peterson:** Data curation. **Carolyn Czerniak:** Data curation, Investigation. **Alexander A. Oliver:** Writing – review & editing, Writing – original draft, Methodology, Data curation. **David F. Kallmes:** Supervision, Resources. **Ramanathan Kadirvel:** Supervision, Resources. **Jeremy E. Schaffer:** Writing – review & editing, Supervision. **Roger J. Guillory:** Writing – review & editing, Writing – original draft, Visualization, Resources, Project administration, Methodology, Investigation, Funding acquisition, Formal analysis, Data curation, Conceptualization.

Acknowledgments

The authors acknowledge the support of Carlo Wolf (School of Mechanical Engineering, University of Applied Sciences Stralsund) for support with the CT analysis and metallographic preparation, Aubrey L. Ehle (Indiana University School of Medicine) for support with the radiopacity assessment, and Amani Gillette (Morgridge Institute for Research) for support with the cytotoxicity analysis. Parts of this study were completed using Michigan Technological University's Applied Chemical and Morphological Analysis Laboratory. RG and NP were partially supported by NIH R15HL167221. AO is supported by American Heart Association grant 23PRE1012781.

Appendix A. Supplementary data

Supplementary data to this article can be found online at https://doi.org/10.1016/j.bioactmat.2024.06.002.

References

[1] M.A. Khan, M.J. Hashim, H. Mustafa, M.Y. Baniyas, S.K.B.M. Al Suwaidi, R. AlKatheeri, F.M.K. Alblooshi, M.E.A.H. Almatrooshi, M.E.H. Alzaabi, R.S. Al Darmaki, Global epidemiology of ischemic heart disease: results from the global burden of disease study, Cureus 12 (7) (2020).

[2] C.W. Tsao, A.W. Aday, Z.I. Almarzooq, A. Alonso, A.Z. Beaton, M.S. Bittencourt, A. K. Boehme, A.E. Buxton, A.P. Carson, Y. Commodore-Mensah, Heart disease and stroke statistics—2022 update: a report from the American Heart Association, Circulation 145 (8) (2022) e153–e639.

[3] J.A. Ormiston, P.W. Serruys, Bioabsorbable coronary stents, Circulation: Cardiovascular Interventions 2 (3) (2009) 255–260.

[4] P. Zartner, R. Cesnjevar, H. Singer, M. Weyand, First successful implantation of a biodegradable metal stent into the left pulmonary artery of a preterm baby, Cathet. Cardiovasc. Interv. 66 (4) (2005) 590–594.

[5] S.-J. Park, S.-J. Kang, R. Virmani, M. Nakano, Y. Ueda, In-stent neoatherosclerosis: a final common pathway of late stent failure, J. Am. Coll. Cardiol. 59 (23) (2012) 2051–2057.

[6] A.A. Oliver, M. Sikora-Jasinska, A.G. Demir, R.J. Guillory II, Recent advances and directions in the development of bioresorbable metallic cardiovascular stents: insights from recent human and in vivo studies, Acta Biomater. 127 (2021) 1–23.

[7] Y.F. Zheng, X.N. Gu, F. Witte, Biodegradable metals, Mater. Sci. Eng. R Rep. 77 (2014) 1–34.

[8] Y. Liu, Y. Zheng, X.H. Chen, J.A. Yang, H. Pan, D. Chen, L. Wang, J. Zhang, D. Zhu, S. Wu, Fundamental theory of biodegradable metals—definition, criteria, and design, Adv. Funct. Mater. 29 (18) (2019) 1805402.

[9] H. Kabir, K. Munir, C. Wen, Y. Li, Recent research and progress of biodegradable zinc alloys and composites for biomedical applications: biomechanical and biocorrosion perspectives, Bioact. Mater. 6 (3) (2021) 836–879.

[10] J. Venezuela, M. Dargusch, Addressing the slow corrosion rate of biodegradable Fe-Mn: current approaches and future trends, Curr. Opin. Solid State Mater. Sci. 24 (3) (2020) 100822.

[11] C. Redlich, P. Quadbeck, M. Thieme, B. Kieback, Molybdenum–a biodegradable implant material for structural applications? Acta Biomater. 104 (2020) 241–251.

[12] G. Song, H.Q. Zhao, Q. Liu, Z. Fan, A review on biodegradable biliary stents: materials and future trends, Bioact. Mater. 17 (2022) 488–495.

[13] M. Jamshidi, M. Rajabian, M.B. Avery, U. Sundararaj, J. Ronsky, B. Belanger, J. H. Wong, A.P. Mitha, A novel self-expanding primarily bioabsorbable braided flow-diverting stent for aneurysms: initial safety results, J. Neurointerventional Surg. 12 (7) (2020) 700–705.

[14] A.A. Oliver, K.D. Carlson, C. Bilgin, J.L.A. Larco, R. Kadirvel, R.J. Guillory, D. D. Daescu, D.F. Kallmes, Bioresorbable flow diverters for the treatment of intracranial aneurysms: review of current literature and future directions, J. Neurointerventional Surg. 15 (2) (2023) 178–182.

[15] A. García, E. Peña, M. Martínez, Influence of geometrical parameters on radial force during self-expanding stent deployment. Application for a variable radial stiffness stent, J. Mech. Behav. Biomed. Mater. 10 (2012) 166–175.

[16] M.R. Jedwab, C.O. Clerc, A study of the geometrical and mechanical properties of a self-expanding metallic stent—theory and experiment, J. Appl. Biomater. 4 (1) (1993) 77–85.

[17] D. Stoeckel, A. Pelton, T. Duerig, Self-expanding nitinol stents: material and design considerations, Eur. Radiol. 14 (2004) 292–301.

[18] S. Dandapat, A. Mendez-Ruiz, M. Martínez-Galdámez, J. Macho, S. Derakhshani, G. F. Torres, V.M. Pereira, A. Arat, A.K. Wakhloo, S. Ortega-Gutierrez, Review of current intracranial aneurysm flow diversion technology and clinical use, J. Neurointerventional Surg. 13 (2021) 54–62.

[19] N. Sasaki, A. Ishii, S. Yagi, H. Nishi, R. Akiyama, M. Okawa, Y. Abekura, H. Tsuji, S. Sakurai, S. Miyamoto, Bioresorbable poly (L-Lactic acid) flow diverter versus cobalt-chromium flow diverter: in vitro and in vivo analysis, Stroke 54 (6) (2023) 1627–1635.

[20] K. Tidwell, S. Harriet, V. Barot, A. Bauer, M.B. Vaughan, M.R. Hossan, Design and analysis of a biodegradable polycaprolactone flow diverting stent for brain aneurysms, Bioengineering 8 (11) (2021) 183.

[21] K. Wang, S. Yuan, X. Zhang, Q. Liu, Q. Zhong, R. Zhang, P. Lu, J. Li, Biodegradable flow-diverting device for the treatment of intracranial aneurysm: short-term results of a rabbit experiment, Neuroradiology 55 (2013) 621–628.

[22] A. Zaccaria, G. Pennati, L. Petrini, Analytical methods for braided stents design and comparison with FEA, J. Mech. Behav. Biomed. Mater. 119 (2021) 104560.

[23] C.G. McKenna, T.J. Vaughan, A finite element investigation on design parameters of bare and polymer-covered self-expanding wire braided stents, J. Mech. Behav. Biomed. Mater. 115 (2021) 104305.

[24] M. De Beule, S. Van Cauter, P. Mortier, D. Van Loo, R. Van Impe, P. Verdonck, B. Verhegghe, Virtual optimization of self-expandable braided wire stents, Med. Eng. Phys. 31 (4) (2009) 448–453.

[25] A.A. Oliver, Y.C. Senol, C. Bilgin, J.E. Schaffer, R. Kadirvel, D.F. Kallmes, J. M. Wainwright, Intraluminal flow diverter design primer for neurointerventionalists, Am. J. Neuroradiol. 45 (4) (2024) 365–370.

[26] P. Nelson, P. Lylyk, I. Szikora, S. Wetzel, I. Wanke, D. Fiorella, The pipeline embolization device for the intracranial treatment of aneurysms trial, Am. J. Neuroradiol. 32 (1) (2011) 34–40.

[27] D. Bradley, L. Kay, H. Lippard, T. Stephenson, Optimization of Melt Chemistry and Properties of 35cobalt-35nickel-20chromium-10molybdenum Alloy Medical Grade Wire, 2003.

[28] J. Schaffer, Mechanical conditioning of superelastic nitinol wire for improved fatigue resistance, J. ASTM Int. (JAI) 7 (5) (2010) 1–7.

[29] L. Pierot, L. Spelle, J. Berge, A.-C. Januel, D. Herbreteau, M. Aggour, M. Piotin, A. Biondi, X. Barreau, C. Mounayer, Feasibility, complications, morbidity, and mortality results at 6 months for aneurysm treatment with the Flow Re-Direction Endoluminal Device: report of SAFE study, J. Neurointerventional Surg. 10 (8) (2018) 765–770.

[30] R.-L. Gao, B. Xu, Z. Sun, C. Guan, L. Song, L. Gao, C. Li, J. Cui, Y. Zhang, K. Dou, First-in-human evaluation of a novel ultrathin sirolimus-eluting iron bioresorbable scaffold: 3-year outcomes of the IBS-FIM trial, Eurointervention: Journal of Europcr in Collaboration with the Working Group on Interventional Cardiology of the European Society of Cardiology EIJ-D (2023).

[31] M. Peuster, C. Hesse, T. Schloo, C. Fink, P. Beerbaum, C. von Schnakenburg, Long-term biocompatibility of a corrodible peripheral iron stent in the porcine descending aorta, Biomaterials 27 (28) (2006) 4955–4962.

[32] M. Peuster, P. Wohlsein, M. Brügmann, M. Ehlerding, K. Seidler, C. Fink, H. Brauer, A. Fischer, G. Hausdorf, A novel approach to temporary stenting: degradable cardiovascular stents produced from corrodible metal—results 6–18 months after implantation into New Zealand white rabbits, Heart 86 (5) (2001) 563–569.

[33] J.-F. Zheng, Z.-W. Xi, Y. Li, J.-N. Li, H. Qiu, X.-Y. Hu, T. Luo, C. Wu, X. Wang, L.-F. Song, Long-term safety and absorption assessment of a novel bioresorbable nitrided iron scaffold in porcine coronary artery, Bioact. Mater. 17 (2022) 496–505.

[34] D. Shen, H. Qi, W. Lin, W. Zhang, D. Bian, X. Shi, L. Qin, G. Zhang, W. Fu, K. Dou, PDLLA-Zn-nitrided Fe bioresorbable scaffold with 53-μm-thick metallic struts and tunable multistage biodegradation function, Sci. Adv. 7 (23) (2021) eabf0614.

[35] G. Sun, W. Guo, H. Zhang, X. Ma, X. Jia, J. Xiong, A novel iron-bioresorbable sirolimus-eluting scaffold device for infrapopliteal artery disease, Cardiovascular Interventions 15 (5) (2022) e57–e59.

[36] W. Lin, H. Zhang, W. Zhang, H. Qi, G. Zhang, J. Qian, X. Li, L. Qin, H. Li, X. Wang, In vivo degradation and endothelialization of an iron bioresorbable scaffold, Bioact. Mater. 6 (4) (2021) 1028–1039.

[37] H. Hermawan, A. Purnama, D. Dube, J. Couet, D. Mantovani, Fe–Mn alloys for metallic biodegradable stents: degradation and cell viability studies, Acta Biomater. 6 (5) (2010) 1852–1860.

[38] A.J. Griebel, J.E. Schaffer, E. Anttila, G. Baker, D.C. Gross, Magnetic susceptibility of common metals and alloys used in medical devices, J. Test. Eval. 51 (6) (2023).

[39] J.E. Schaffer, E.A. Nauman, L.A. Stanciu, Cold-drawn bioabsorbable ferrous and ferrous composite wires: an evaluation of mechanical strength and fatigue durability, Metall. Mater. Trans. B 43 (2012) 984–994.

[40] J.E. Schaffer, Biodegradable Alloy Wire for Medical Devices, European Patent 2872663B1, (2020).

[41] A.A. Oliver, C. Bilgin, A.J. Vercnocke, K.D. Carlson, R. Kadirvel, R.J. Guillory, A. J. Griebel, J.E. Schaffer, D. Dragomir-Daescu, D.F. Kallmes, Benchtop proof of concept and comparison of iron-and magnesium-based bioresorbable flow diverters, J. Neurosurg. 1 (aop) (2022) 1–7.

[42] A. Oliver, E. Koons, P. Trester, J. Kleinow, R. Jonsgaard, A. Vercnocke, C. Bilgin, R. Kadirvel, S. Leng, A. Lu, Medical imaging compatibility of magnesium-and iron-based bioresorbable flow diverters, Am. J. Neuroradiol. 44 (6) (2023) 668–674.

[43] ASTM F640, ASTM International, Standard Test Methods for Determining Radiopacity for Medical Use.

[44] B.L. Belanger, R. Morrish, D. McClarty, C. Barnstable, W. Muir, S. Ghazizadeh, M. Eesa, D. Fiorella, J.H. Wong, C. Sadasivan, In vitro flow diversion effect of the ReSolv stent with the shelf technique in a bifurcation aneurysm model, J. Neurointerventional Surg. 16 (3) (2024) 296–301.

[45] J.E. Schaffer, DFT biocompatible wire, Adv. Mater. Process. 160 (10) (2002) 51.

[46] A. Boese, G. Rose, M. Friebe, T. Hoffmann, S. Serowy, M. Skalej, W. Mailänder, G. Cattaneo, Increasing the visibility of thin NITINOL vascular implants, Current Directions in Biomedical Engineering 1 (1) (2015) 503–506.

[47] M.S. Michael, H.-J. Wachter, R.J. Myers, Drawn strand filled tubing wire, U.S. Patent 7745732B2 (2010).

[48] J.E. Schaffer, Biodegradable Composite Wire for Medical Devices, U.S. Patent 9561308B2, (2017).

[49] A.J. Griebel, J.E. Schaffer, Absorbable Filament Technologies: Wire-Drawing to Enable Next-Generation Medical Devices, Magnesium Technology, 2016, pp. 323–327, 2016.

[50] M. Sikora-Jasinska, L.M. Morath, M.P. Kwesiga, M.E. Plank, A.L. Nelson, A. A. Oliver, M.L. Bocks, R.J. Guillory II, J. Goldman, In-vivo evaluation of molybdenum as bioabsorbable stent candidate, Bioact. Mater. 14 (2022) 262–271.

[51] J.E. Schaffer, Fatigue Damage Resistant Wire and Method of Production Thereof, U.S. Patent 8840735B2, (2014).

[52] D. Dabir, A. Feisst, D. Thomas, J.A. Luetkens, C. Meyer, A. Kardulovic, M. Menne, U. Steinseifer, H.H. Schild, D.L. Kuetting, Physical properties of venous stents: an experimental comparison, Cardiovasc. Intervent. Radiol. 41 (2018) 942–950.

[53] R.J. Guillory, A.A. Oliver, E.K. Davis, E.J. Earley, J.W. Drelich, J. Goldman, Preclinical in vivo evaluation and screening of zinc-based degradable metals for endovascular stents, Jom 71 (2019) 1436–1446.

[54] A.A. Oliver, Y.C. Senol, C. Bilgin, J.E. Schaffer, R. Kadirvel, D.F. Kallmes, J. M. Wainwright, Intraluminal flow diverter design primer for neurointerventionalists, Am. J. Neuroradiol. 45 (4) (2024) 365–370.

[55] H. Wang, Y. Zheng, J. Liu, C. Jiang, Y. Li, In vitro corrosion properties and cytocompatibility of Fe-Ga alloys as potential biodegradable metallic materials, Mater. Sci. Eng. C 71 (2017) 60–66.

[56] H.Y. Ang, D. Toong, W.S. Chow, W. Seisilya, W. Wu, P. Wong, S.S. Venkatraman, N. Foin, Y. Huang, Radiopaque fully degradable nanocomposites for coronary stents, Sci. Rep. 8 (1) (2018) 17409.

[57] D. Mei, S.V. Lamaka, X. Lu, M.L. Zheludkevich, Selecting medium for corrosion testing of bioabsorbable magnesium and other metals–a critical review, Corrosion Sci. 171 (2020) 108722.

[58] J.E. Schaffer, Development and Characterization of Vascular Prosthetics for Controlled Bioabsorption, Purdue University, 2012.

[59] C. Redlich, A. Schauer, J. Scheibler, G. Poehle, P. Barthel, A. Maennel, V. Adams, T. Weissgaerber, A. Linke, P. Quadbeck, In vitro degradation behavior and biocompatibility of bioresorbable molybdenum, Metals 11 (5) (2021) 761.

[60] R. Waksman, R. Pakala, R. Baffour, R. Seabron, D. Hellinga, F.O. Tio, Short-term effects of biocorrodible iron stents in porcine coronary arteries, J. Intervent. Cardiol. 21 (1) (2008) 15–20.

[61] J.E. Schaffer, E.A. Nauman, L.A. Stanciu, Cold drawn bioabsorbable ferrous and ferrous composite wires: an evaluation of in vitro vascular cytocompatibility, Acta Biomater. 9 (10) (2013) 8574–8584.

[62] P.P. Mueller, T. May, A. Perz, H. Hauser, M. Peuster, Control of smooth muscle cell proliferation by ferrous iron, Biomaterials 27 (10) (2006) 2193–2200.

[63] A. Schauer, C. Redlich, J. Scheibler, G. Poehle, P. Barthel, A. Maennel, V. Adams, T. Weissgaerber, A. Linke, P. Quadbeck, Biocompatibility and degradation behavior of molybdenum in an in vivo rat model, Materials 14 (24) (2021) 7776.